Shallow crustal imaging using distant, high-magnitude earthquakes

Van IJsseldijk, Johno; Ruigrok, Elmer; Verdel, Arie; Weemstra, Cornelis

DOI
10.1093/gji/ggz343

Publication date
2019

Document Version
Final published version

Published in
Geophysical Journal International

Citation (APA)
Van IJsseldijk, J., Ruigrok, E., Verdel, A., & Weemstra, C. (2019). Shallow crustal imaging using distant, high-magnitude earthquakes. *Geophysical Journal International*, *219*(2), 1082-1091. https://doi.org/10.1093/gji/ggz343

Geophysical Journal International

Geophys. J. Int. (2019) **219,** 1082–1091
Advance Access publication 2019 July 26
GJI Seismology

doi: 10.1093/gji/ggz343

Shallow crustal imaging using distant, high-magnitude earthquakes

Johno van IJsseldijk [1,*] Elmer Ruigrok [2,3] Arie Verdel [4] and Cornelis Weemstra [1,3]

[1] *Department of Geoscience and Engineering, Delft University of Technology, Delft, The Netherlands. E-mail: J.E.vanIJsseldijk@tudelft.nl*
[2] *Department of Earth Sciences, Utrecht University, Utrecht, The Netherlands*
[3] *Royal Netherlands Meteorological Institute, De Bilt, The Netherlands*
[4] *Netherlands Organisation for Applied Scientific Research TNO, Utrecht, The Netherlands*

Accepted 2019 July 25. Received 2019 July 23; in original form 2019 February 8

SUMMARY

Global phases, viz. seismic phases that travel through the Earth's core, can be used to locally image the crust by means of seismic interferometry. This method is known as Global Phase Seismic Interferometry (GloPSI). Traditionally, GloPSI retrieves low-frequency information (up to 1 Hz). Recent studies, however, suggest that there is high-frequency signal present in the coda of strong, distant earthquakes. This research quantifies the potential of these high-frequency signals, by analysing recordings of a multitude of high-magnitude earthquakes ($\geq$6.4 M_w) and their coda on a selection of permanent USArray stations. Nearly half of the *P*, *PKP* and PKIKP phases are recorded with a signal-to-noise ratio of at least 5 dB at 3 Hz. To assess the viability of using the high-frequency signal, the second half of the paper highlights two case studies. First, a known sedimentary structure is imaged in Malargüe, Argentina. Secondly, the method is used to reveal the structure of the Midcontinent Rift below the SPREE array in Minnesota, USA. Both studies demonstrate that structural information of the shallow crust ($\leq$5 km) below the arrays can be retrieved. In particular, the interpreted thickness of the sedimentary layer below the Malargüe array is in agreement with earlier studies in the same area. Being able to use global phases and direct *P*-phases with large epicentral distances ($>80^\circ$) to recover the Earth's sedimentary structure suggests that GloPSI can be applied in an industrial context.

Key words: Body wave; Crustal imaging; Seismic interferometry.

1 INTRODUCTION

Claerbout (1968) found that the 1-D reflection response of a layered medium can be retrieved by autocorrelation of the transmission response of the medium due to an incident plane-wave. This finding forms the basis of reflected-wave interferometry (Wapenaar *et al.* 2010). Ruigrok & Wapenaar (2012) then adapted this theory for use in global-scale seismology, resulting in Global-Phase Seismic Interferometry (GloPSI). The method retrieves the reflection response of the medium from the transmission response of global phases, viz. earthquake phases that have traveled through the Earth's core before reaching a receiver (such as *PKP*- and *PKIKP*-phases; Storchak *et al.* 2003). For the application of GloPSI, seismicity can be used over a large area at the other side of the globe. The vertical component already provides a relatively accurate estimate of the reflection response.

Although GloPSI has been used to obtain images of the upper mantle and crust (e.g. Ruigrok & Wapenaar 2012; Nishitsuji *et al.* 2016), these studies were performed in relatively low-frequency bands (0.04–1 Hz). Imaging the shallow crust, however, requires higher frequencies to be included, in order to improve the vertical resolution of the sections. This raises the question whether shallow crustal imaging can be achieved with GloPSI.

This study is partly inspired by results from another technique that is also largely based on the results by Claerbout (1968), known as Ambient Noise Seismic Interferometry (ANSI). The application of ANSI to retrieve body waves, used in geophysical exploration and monitoring, is known to provide valuable reflection information of the shallow crust up to depths of $\sim$1 km (e.g. Draganov *et al.* 2007, 2009, 2013; Boullenger *et al.* 2015). ANSI can also provide valuable reflection information at much larger depths: Moho-reflected *P* waves (PmP) were retrieved from ANSI-crosscorrelations by Ruigrok *et al.* (2011) and Poli *et al.* (2012), and Moho reflected *S* waves were retrieved by Zhan *et al.* (2010). Whereas ANSI-autocorrelations for frequencies up to 0.55 Hz were used by Oren & Nowack (2017) to estimate crustal thickness, Tibuleac & von Seggern (2012) retrieved Moho-reflected *P* and *S* waves (SmS) from ANSI-autocorrelations using frequencies up to 1 Hz.

* The author performed this work at: Netherlands Organisation for Applied Scientific Research TNO, Utrecht, The Netherlands.

Autocorrelations of ambient noise with frequencies in the range 1.0–2.0 Hz were used by Becker & Knapmeyer-Endrun (2018) to map crustal thickness. Gorbatov *et al.* (2013) and Kennett *et al.* (2015) autocorrelated ambient noise in the 2.0–4.0 Hz range to identify PmP. The same frequency band was used by Saygin *et al.* (2017) to determine basin-depth; their results indeed provided reflection information at shallow crustal scale. Even more recently, higher frequencies, up to 8 Hz, were used by Heath *et al.* (2018) to determine internal volcano structure and, finally, Romero & Schimmel (2018) employed frequencies up to 18 Hz to map the basement of the Ebro basin with autocorrelations of ambient noise.

Based on this overview of ANSI examples, it can be concluded that the frequency band for which ANSI can be applied successfully for delineation of intracrustal reflectors has broadened largely. In particular, the frequency-band has widened for ANSI-autocorrelations, and applications now range from exploration-scale depth (up to a few km) at the high-frequency end to mantle-scale depth at the low-frequency end. It should be noted that even though the frequency-band has broadened for ANSI-autocorrelations, successful application of ANSI is dependent on the location and season, as sufficient body wave coverage and energy in the ambient seismic field is required.

Ideally, a similar scale-range broadening for crustal imaging can be achieved for GloPSI. A positive indication for this broadening was obtained recently: while looking for means to compare the reflections retrieved from ANSI-autocorrelations in a study to determine the geothermal reservoir structure at the Reykjanes peninsula (Iceland), Verdel *et al.* (2016) observed high-frequency signal (up to 8 Hz) while applying GloPSI to a strong, teleseismic (90°) earthquake. This result appeared to show remarkable correspondence with the ANSI result for a variety of broadband stations and one short period station for depths ranging from 1 to 3 km. This observation triggered this study, which aims to quantify the occurrence of this high-frequency signal and evaluate if GloPSI can indeed be used more widely to retrieve structural information of the shallow crust. Recent work from Saygin & Kennett (2019) found body wave reflections, in the frequency band from 1 to 5 Hz, in the coda of *P* and *S* phases at regional distances. If similar frequencies are found in global phases, GloPSI could potentially be used to image the upper crust.

Furthermore, the possibility of including other teleseismic phases in GloPSI is examined. The larger ray parameter of these phases can potentially aid the method in the imaging of dipping structures. In a recent study, Phạm & Tkalčić (2018) imaged the thickness of the Antarctic ice using autocorrelations of both global and teleseismic phases.

The first half of the paper addresses quantifying the amount of high-frequency signal. In order to do this, a number of permanent stations from the USArray are selected, that have been recording since at least 2011. This long lifespan ensures that a multitude of high-magnitude events can be analysed. In the second half of the paper, we present two case studies in which we evaluate whether the high-frequency signal is actually suitable for retrieving structural information. The first study uses data recorded by the Malargüe array in Argentina, which is located on top of a sedimentary basin (Ruigrok *et al.* 2012; Weemstra *et al.* 2017). In the second case study we utilize data recorded by the SPREE array, which is located on top of the Midcontinent Rift in Minnesota and Wisconsin (Stein *et al.* 2011; Van der Lee *et al.* 2013).

2 THEORY

Reflected-wave seismic interferometry is based on the 1-D derivation by Claerbout (1968), who showed that by autocorrelation of the transmission response due to an impulsive source at depth one can obtain the reflection response. This is shown graphically in Fig. 1. Imagine the situation where a plane wave is radiated from the lower half-space below a free surface with a single reflector in the subsurface as shown in Fig. 1(a). The transmission response measured at the surface is given in Fig. 1(b); here the amplitude of the first peak is equal to τ_1. The amplitude of the consecutive arrivals is obtained by multiplying with $-r_1$ each time (note that for the free surface $r_0 = -1$). The reverse of the autocorrelation of the transmission response reveals a causal and anticausal reflection response as well as a negative delta pulse at $t = 0$ as shown in Fig. 1(c): the first peak in the reflection response has an amplitude of r_1, again consecutive peaks (free surface multiples) are obtained by multiplying with $-r_1$. Eq. (1) shows how this concept can be written in a more general form (Wapenaar *et al.* 2010):

$$R(t) + R(-t) - \delta(t) = -T(t) * T(-t). \tag{1}$$

Figs 1(b) and (c) are illustrations of the right-hand and left-hand side, respectively. In eq. (1) $R(+t)$ and $R(-t)$ denote the causal and anticausal reflection response, respectively, $\delta(t)$ the Dirac delta function and T the transmission response. The in-line asterisk $*$ denotes temporal convolution. This equation, however, is only valid for perfectly horizontally layered media and a delta pulse source function, which is rarely the case in reality. Therefore, eq. (1) needs to be adapted in order to include slightly dipping layers. This is done by stacking over events with different ray parameters and azimuths. Furthermore, to account for real source signatures both sides of the equation are convolved with a source time function. Consequently, eq. (1) now reads (Ruigrok & Wapenaar 2012):

$$\{R(t) + R(-t) - \delta(t)\} * S_n(t) \propto \sum_{\theta_{min}}^{\theta_{max}} \sum_{p_{min}}^{p_{max}} -T(\boldsymbol{p}, -t) * s_i(-t) * T(\boldsymbol{p}, t) * s_i(t). \tag{2}$$

Here $\boldsymbol{p} = (p, \theta)$, with p the absolute horizontal ray parameter and θ the back azimuth. $s_i(t)$ is the source time function of the ith source and $S_n(t)$ is the average of all autocorrelations of the source time functions. This is illustrated for a single source in Fig. 1, where the source time function (a 25 Hz Ricker wavelet) of the transmission response (Fig. 1b) turns into an autocorrelation of itself in the retrieved reflection response (Fig. 1c). The summations on the right-hand side imply stacking. The stacking does not only allow for the detection of dipping layers by illumination from multiple angles as stated before, but it also suppresses source-side effects (Ruigrok *et al.* 2010). In this study we will only consider ray parameters smaller than 0.045 s km^{-1} (i.e. $p_{\max} \leq 0.045$ s km^{-1}), in order to ensure that the signal contains information about the reflectivity (almost) directly below the station. Compared to earlier studies (e.g. Ruigrok & Wapenaar 2012; Nishitsuji *et al.* 2016) this ray parameter limit is slightly higher, allowing to include additional teleseismic events, namely *P*-phase events originating at a distance of at least 80°.

3 ANALYSIS OF THE SPECTRUM OF THE EARTHQUAKE CODA

In order to assess the amount of high-frequency signal, 21 USArray permanent stations, active since at least 2011, have been selected.

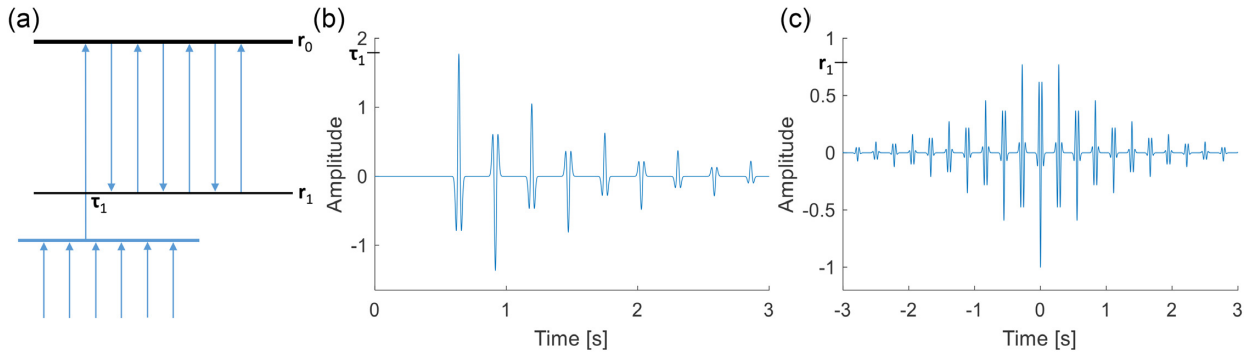

Figure 1. Principle of GloPSI. (a) Simple medium with a free surface (r_0), a single reflector (r_1), and an upgoing plane wave impinging from below. (b) The transmission response due to the plane wave measured at the free surface. (c) The reverse of the autocorrelation of the transmission response reveals the reflection response, which is represented by the causal part, as well as a negative delta pulse at $t = 0$. The figure is inspired by Wapenaar *et al.* (2010).

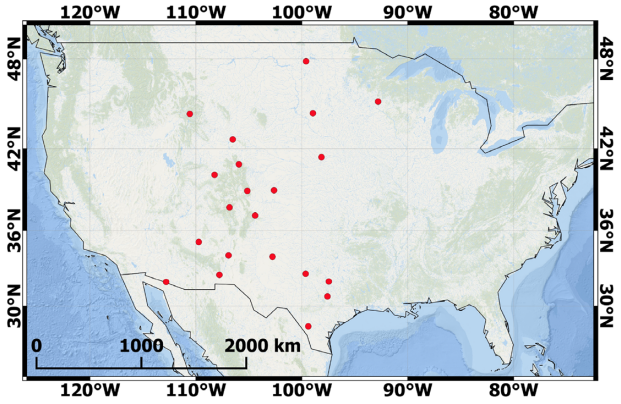

Figure 2. The location of the 21 selected USArray stations. Basemap retrieved from ESRI (2014).

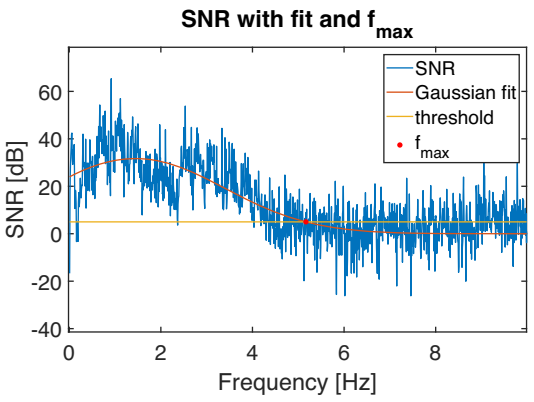

Figure 3. SNR for the event (blue), a Gaussian fit (red) is used to approximate and smooth the SNR. The intersection with the threshold of 5 dB (yellow) with this fit marks the maximum frequency (red dot).

The long lifespan of these stations implies that a large number of earthquakes have been recorded; over 2000 earthquakes with a magnitude >6.4 occurred from the first recording in 2008 until April 2018. Since individual earthquakes were recorded at multiple stations, more than 10 000 seismograms can be analysed. The location of the selected stations is shown in Fig. 2. The data acquisition and processing will be discussed in the next sections. In addition, a flowchart summarizing these sections is provided in the supporting information (Fig. S1).

3.1 Data acquisition

Earthquake, as well as station data, are retrieved from the IRIS (Incorporated Research Institutions for Seismology) database. For each earthquake, the expected first arrival and ray parameter are calculated using the TauP toolkit (Crotwell *et al.* 1999) with the IASP91 model (Kennet 1991). Next, the waveform information at each station is retrieved, starting 5 min before the arrival time of the first phase and ending 25 min after its arrival. Finally, the signal is deconvolved with the instrument response of the station, which converts from raw data in digital counts to vertical particle velocities in $\mathrm{m\,s^{-1}}$. From the deconvolved signal the arrival time of each identified phase, i.e. existing at the particular epicentral distance, is determined. Subsequently, the first arrival of each phase, together with 2 min of coda, is used as input signal for further analysis. This signal is equivalent to the transmission response convolved with the source time function in eq. (2). Because multiple phases may arrive within the same 25 min window, multiple signal windows may be selected.

3.2 Data processing

The maximum frequency (denoted by f_{max}) is the frequency at which there is still significant useful energy present in the main phase arrival and subsequent coda. This will be defined by the frequency at which the signal-to-noise ratio (SNR) is still greater than 5 dB. As stated before, the signal starts with the first arrival and stops 2 min thereafter. For the noise, the first 2 min of the recording, which starts 5 min before the arrival of the first phase, is selected. After Fourier decomposition, the SNR, based on signal power, is computed for every frequency sample. Subsequently, this SNR is fitted (in least-squares sense) with a Gaussian function. From this fit, f_{max} is determined by evaluating the intersection of the fit and the 5 dB threshold. An example of the fit of a 6.9 M_{w} earthquake is provided in Fig. 3. The event occurred on the 18th of February 2010 at a depth of almost 575 km and was located just southwest of Vladivostok, Russia. At 01:24:55 UTC the first arrival (*P*-phase) was recorded by USArray station 214A in Arizona, at an approximate distance of 85° from the earthquake location.

Another parameter that is considered is the corner frequency (f_c). Although this parameter is not directly used for GloPSI, it does provide valuable insights in the quality of the data. Together with long-period spectral level (Ω_0), the corner frequency determines the energy in the far-field displacement spectrum (Shearer 2009).

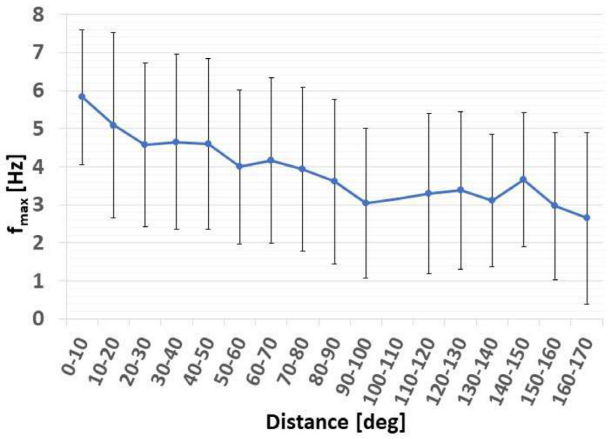

Figure 4. Mean of the maximum frequency versus distance. In total 6865 *P*-, *PKP*- and *PKIKP*-phases ($M_w \geq 6.4$), recorded by the selected USArray stations, were considered. For distances of 100–110° none of the selected phases are available. One side of the error bars is equal to 1 standard deviation.

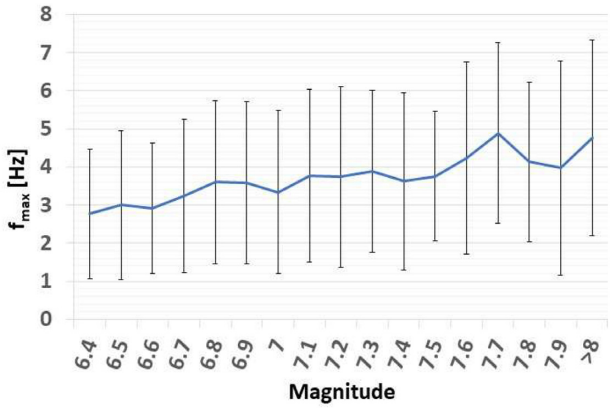

Figure 5. Mean of the maximum frequency versus magnitude. In total 4082 *P*-, *PKP*- and *PKIKP*-phases were considered, with an event-station distance of at least 80° and a moment magnitude of at least 6.4. One side of the error bars is equal to 1 standard deviation.

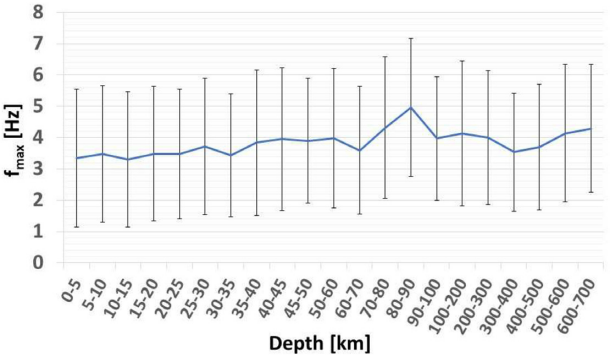

Figure 6. Mean of the maximum frequency versus depth. Note that the bin size increases with depth, to ensure that each bin contained at least 50 phase recordings. In total 6865 *P*-, *PKP*- and *PKIKP*-events ($M_w \geq 6.4$), recorded by the selected USArray stations, were considered. One side of the error bars is equal to 1 standard deviation.

Ω_0 determines the initial level of the spectrum, while the corner frequency indicates the frequency at which the amplitude starts decaying in the displacement spectrum. For increasing earthquake magnitude, Ω_0 increases while the corner frequency decreases. A stronger earthquake, therefore, has more spectral energy at low frequencies, but the energy decay of the spectrum also starts at lower frequencies. Thus, it is not straightforward whether a larger earthquake also produces more energy at high frequencies. The corner frequency is approximated by fitting the retrieved amplitude spectra of the earthquakes according to Dost *et al.* (2018). These authors provide a model to predict the displacement spectrum ($A(f)$), which is the product of a source term, an attenuation term, and a site-specific term:

$$A(f) = \frac{\Omega_0}{(1 + (f/f_c)^4)^{1/2}} S(f) e^{-\pi f t^*}. \quad (3)$$

Here Ω_0 is the long-period spectral level mentioned earlier. The ratio accounts for the source-side effects, according to the source model proposed by Boatwright (1978). The second term, $S(f)$, is for receiver-site-specific effects. Finally, the exponential term with t^* accounts for propagation and attenuation in the Earth. Since, the corner frequency of high-magnitude earthquakes should be significantly smaller than 1 Hz (Madariaga 1976; Shearer 2009), any events with a corner frequency exceeding 1 Hz are discarded.

3.3 Maximum frequency

In the remainder of this study (i.e. also for the case studies), only the *P*-, *PKP*- and *PKIKP*-phases are considered. Due to the absence of surface bounce points and diffractions along their paths, these phases can be expected to be most energetic. Consequently, the f_{max} associated with these phases can be expected to be relatively high. In addition, the ray parameter of these phases is mostly below 0.045 s km^{-1} at distances greater than 80°. Moreover, they arrive prior to the arrival of *S* and surface waves, therefore, these phases experience minimal interference with other phases. Fig. 4 shows the maximum frequency as a function of distance. These results are based on 6865 measurements by the USArray stations (Fig. 2). Note that there is a global trend in the value of f_{max}, which is decreasing for increasing distances. This is to be expected since, in general, longer distances imply more attenuation losses. At 140–150° a peak is observed, which is due to *PKP*-triplications at this distance. Furthermore, the trough at 90–100° can be explained as well; this is where the transition from the *P*-phase to Pdiff occurs.

For this study, only the events with a distance of at least 80° are considered since these remain under the maximum ray parameter limit of 0.045 s km^{-1}. Fig. 5 displays f_{max} versus magnitude, for events with a minimum distance of 80°, leaving a total of 4082 available events. This graph provides valuable insights into the expected value of f_{max} since the selection criteria are the same as those that will be used for GloPSI. Note that the f_{max} is increasing with magnitude, and that the mean value is mostly greater than 3 Hz. This is promising for the application with GloPSI since it is significantly larger than the hitherto GloPSI maximum of 1 Hz. Furthermore, the standard deviation appears to increase with increasing magnitudes. This is likely due to the fact that large earthquakes are rarer, meaning there are fewer data available (e.g. over 600 magnitude 6.4 events are recorded, but less than 50 magnitude 8+ events).

Finally, the relation between f_{max} and the depth of the earthquakes is studied. The results are shown in Fig. 6. Note that the bin size increases with depth, in order to have sufficient events in each bin (i.e. more than 50 phase recordings). In Fig. 6 a trend is observed, namely that with increasing depth the f_{max} also increases. This trend is likely to be caused by the shorter paths (from source to receiver) travelled

by the phases, meaning that there is less geometrical spreading and intrinsic attenuation in the subsurface. In addition, in the crust (0 to ∼45 km), a lot of scattering causes additional attenuation, and therefore lower f_{max}, is expected. This is confirmed by the figure, as the frequencies increase from 3.3 Hz at 0–5 km depth to almost 4 Hz at depths larger than 40 km. However, the differences in frequencies for different depths are not as large as those observed with distance and magnitude in earlier figures.

4 CASE STUDIES

In the previous section, it was concluded that for large magnitude events a relatively high f_{max} is expected. By considering two seismic arrays, we will, in this section, validate whether this observation can be used to image the upper crust. The data acquisition and window selection are the same as for the USArray. Next, suitable events are selected, based on the ray parameter ($p \leq 0.045$ s km^{-1}) and corner frequency ($f_c \leq 1$) criteria. From the selected data, a threshold frequency f_{th} is determined for each station. This threshold frequency is defined as that frequency for which a total of n events have an $f_{max} > f_{th}$. For a specific n, f_{th} varies per station because (i) not all stations have recorded all events (due to gaps in the data), (ii) the subsurface is laterally varying and (iii) different stations have different noise characteristics. Clearly, there exists a trade-off between n and f_{th}: where we want to select a large number of events for the purpose of GloPSI (i.e. events that fulfill the criteria regarding ray parameter and corner frequency), f_{th} necessarily decreases. Subsequently, we apply spectral whitening to the individual traces. In practice, this is achieved by means of a normalization of each spectral sample by the mean amplitude in a narrow frequency band (0.75 Hz) surrounding the frequency associated with that sample. The last step before autocorrelation is band-pass filtering. The upper cutoff frequency is set to the lowest f_{th} of the seismic array of interest for the case study. The lower cutoff frequency is determined such that the frequency band spans at least one octave. Finally, the individual autocorrelations are computed and normalized by their maximum (time-domain) amplitude, prior to the n-fold stacking. This process is repeated for all stations of the seismic array of interest, resulting in 2-D seismic sections. A concise overview of the processing is provided in the supporting information (Fig. S2).

4.1 Malargüe array

The Malargüe T-Array is located in Argentina, east of the Andean Mountain range. The array consists of 32 short-period stations active during 2012. The array is located on top of the Malargüe basin, a sedimentary syntectonic structure, situated east of the north–south Malargüe Anticline fold axis (Kraemer *et al.* 2011; Weemstra *et al.* 2017). The TN-line (north–south) is located about 10 km east of, and in parallel to, this fold axis, whereas the TE-line (east–west) is perpendicular to the axis, with the first station at a distance of about 25 km (Fig. 7). The sedimentary thickness of the basin infill is decreasing towards the east (Kraemer *et al.* 2011; Nishitsuji *et al.* 2014). Nishitsuji *et al.* (2014) concluded this, based on the application of the global phase H/V spectral ratio (GloPHV) method to the Malargüe array. These authors find that the average thickness below the TN-line is about 5 km and that the thickness at the first TE-station is about 4 km and decreases to about 500 m below the easternmost station of the line.

The coverage of *P*-phases with high f_{max} for the Array was extremely sparse, and, using only *P* phases, an f_{th} >3 Hz could not

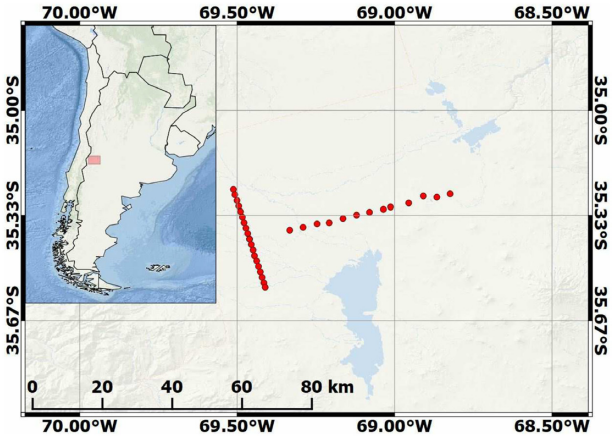

Figure 7. Location of the Malargüe T-array. The TE-line extends from east to west, whereas the TN-line extends from north to south. The inset shows the relative location of the array. Basemap retrieved from ESRI (2014).

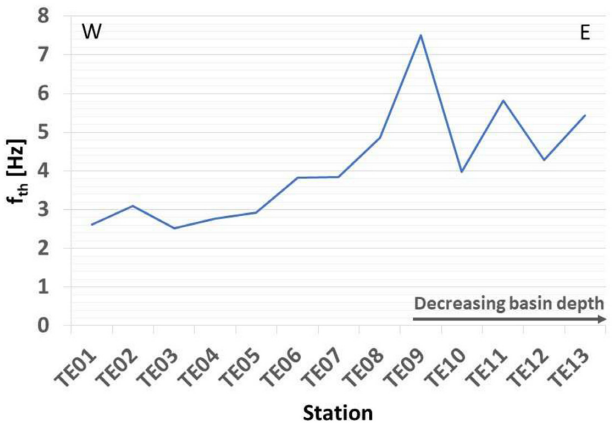

Figure 8. Lowest f_{th} used in the stacking fold ($n = 10$) for each station of the TE-line. The westernmost stations (TE01–TE05) have a significantly lower f_{th} compared to the easternmost stations (TE08–TE13).

be achieved for all stations even at a stacking-fold of $n = 1$. Consequently, only *PKIKP*-phases are considered for autocorrelation. The stacking-fold (n) for the Malargüe array is set to 10, as this allowed to use many stations while still achieving a f_{th} close to 3 Hz. In Fig. 8 the f_{th} for each station are displayed. Station TE01 is the first, westernmost station of the line, and TE13 is the easternmost station. Interestingly, the stations in the west have a lower f_{th} compared to the eastern stations. This may be explained by a thicker sedimentary layer, resulting in more intrinsic attenuation at higher frequencies.

Fig. 9 shows the individual autocorrelations of the *PKIKP*-phases for stations TE02, TE07 and TE13, as well as the final stack for each station. The autocorrelations are whitened, as described before, and a 4th-order Butterworth filter between 0.7 and 3 Hz is applied. Finally, the individual autocorrelations are summed to obtain the final stack (displayed in red). On the vertical axis the two-way traveltime (TWT) is displayed, e.g. the time it takes for a body wave to travel down to the reflector and then up to the surface again. The black arrow represents the interpreted depth of the basin, which is deepest below station TE02 and non-existent below station TE13. Note, that the individual autocorrelations also display a lot of wiggles below the basin depth, however, in the final stack these events are weakened. The common events that are shared by all

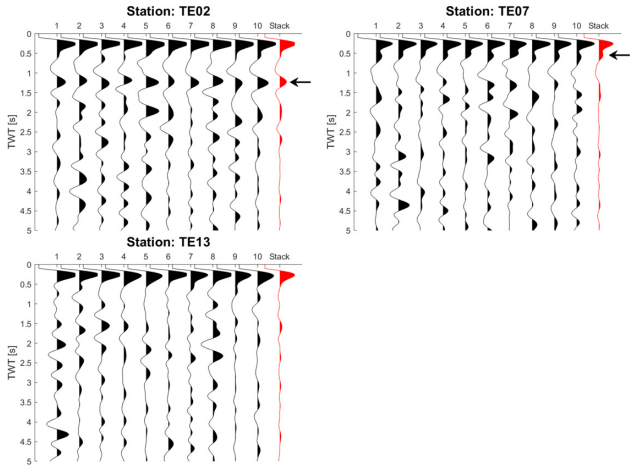

Figure 9. The autocorrelated traces for single *PKIKP*-events (black) as well as the final stack (red) for three of stations on the TE-line. The black arrow indicates the interpreted basin depth. Note that station TE13 is situated to the side of the basin.

autocorrelations are not affected; this implies that stacking has the desired effect of removing source-side signatures, whereas receiver-side effects stack constructively.

The final autocorrelation result for the Malargüe array is displayed in Fig. 10; a dipping structure below the TE-line is clearly observed in this figure. The TWT is converted to depth rather crudely, using a constant *P*-wave velocity of 5.2 km s^{-1} (e.g. Farías *et al.* 2010). Compared to the results by Nishitsuji *et al.* (2014), the results presented here show a slightly thinner sedimentary unit. To get a better estimate of the depth, a better velocity model would be desired. The structure of the basin, however, is almost identical for both studies. The depth of the basin roughly corresponds to the interface between the sandstone of the Neuquén Group and the Permian-Triassic andesite of the Choiyoi Group (Kraemer *et al.* 2011). We would indeed expect a strong contrast between these layers due to a relatively large difference in the elastic properties of the constituent rocks.

In Fig. 10, positive amplitudes, corresponding with an acoustic-impedance increase with depth, are shown in red and negative amplitudes in blue. The positive (red) structure in the figure is identified as the bottom of the basin. The positive (red) amplitudes are accompanied by neighbouring blue amplitudes, these can be interpreted as the sidelobes of the spatial wavelet that has limited vertical resolution. The location where the dipping structure of the TE-line reaches the surface, seems to coincide with a mountainous structure in the topography. This suggests that the dipping layer surfaces at this location. Furthermore, the approximate depth of the basin at the westernmost stations of the TE-line is 3.7 km, whereas the depth at the extrapolated intersection with the TN-line is equal to 4.5 km. In addition, the northern-most part of the TN-line the signal is slightly distorted and interpretation of the basin depth is harder; earlier studies show a similar disturbance at these stations (Nishitsuji *et al.* 2014; Weemstra *et al.* 2017).

Finally, we note that Ruigrok & Wapenaar (2012) subtracted the scaled average of all autocorrelograms from the stack of each station in order to further suppress source-side effects. This requires that the array crosses a highly heterogeneous subsurface. A similar approach applied to the Malargüe array improves the results below the TE-line, which is indeed heterogeneous. The result below the TN-line, however, deteriorates, as it crosses relatively laterally homogeneous geology. These results are shown in Figs S5 and S6 of the supporting information.

4.2 SPREE array

The second seismic array we consider is the SPREE-array, located in Minnesota and Wisconsin, USA. The array is designed to get a better understanding of the Midcontinent Rift (MCR) (Stein *et al.* 2011). The array consists of 83 broad-band stations, of which 67 are located in the US and 16 in Canada. These stations recorded continuously from April 2011 to October 2013 (Wolin *et al.* 2015). The U.S. stations are subdivided into three lines: SN in the north, SM in the middle and SS in the south as shown in Fig. 11. In this study, we only consider the SN-stations, which are displayed as green dots in the figure. The SN-line starts with station SN43 in the northwest and ends with station SN63 in the southeast. These stations are perpendicular to a gravity anomaly marking the MCR (Stein *et al.* 2011). Stations SN52 to SN56 are located right on top of the gravity anomaly (Zhang *et al.* 2016).

The rifting of the MCR occurred 1.1 Ga ago (Hinze *et al.* 1997); the exact cause for the formation of the rift is up for debate. Both active rifting caused by a mantle plume (Hutchinson *et al.* 1990) and passive rifting linked to the Grenville Orogeny (Gordon & Hempton 1986) have been suggested. This extensional regime strongly thinned the crust, but failed to separate the continent. The formed basin later was filled with sediments and a compressional regime resulted in reverse faults (Hinze *et al.* 1997). Presently, only the gravity and magnetic anomalies (King & Zietz 1971; Keller *et al.* 1980) point at the presence of the rift below the relatively flat surface. This study aims to image the main structural features of this rift.

Contrary to the Malargüe array, there were more *P*-phases available from events at at-least 80° epicentral distance, mostly originating from central Chile and Japan, allowing application of GloPSI with *P*-, *PKP*- and *PKIKP*-phases. This addition allows for a lowest f_{th} of 2.60 Hz and a highest f_{th} of 5.53 Hz with a total stacking fold of $n = 30$. Moreover, since the SN-line is crossing heterogeneous subsurface, the scaled average of the autocorrelations is subtracted from the final stack of each station. Fig. 12 shows the final results for the SN-line using both *P*- and *PKIKP*-phases. Again, a rather crude conversion from TWT to depth was applied, using a constant velocity of 6.4 km s^{-1} (Chulick & Mooney 2002).

Of particular interest in Fig. 12 is the dim spot located below stations SN52 to SN54, which coincides with the location of the MCR. The cause of this dim spot is likely due to the lower reflectivity of the volcanic rocks of the MCR compared to the surrounding Precambrian crust. The interfaces around this dim spot appear to be dipping towards the MCR, which is an indication for the presence of a graben structure. Similar structures were found for the MCR below the lake superior region (Shay & Tréhu 1993), as well as below the SPREE array itself (Zhang *et al.* 2016). The subtraction of the scaled average reveals additional features at near-surface depths (e.g. the first few kilometers), similarly as previously shown for TE-line of the Malargüe array (Figs S3 and S5). This allows for comparison of our results with the sedimentary depths found by Zhang *et al.* (2016). Below the MCR and to the east of the MCR similar structures are found by both studies. However, the base of the sediments towards the west of the MCR is steeply dipping (Zhang *et al.* 2016) and these dipping interfaces are not captured by the GloPSI results, due to the limited ray parameter band that is used ($p \leq 0.045$ s km^{-1}).

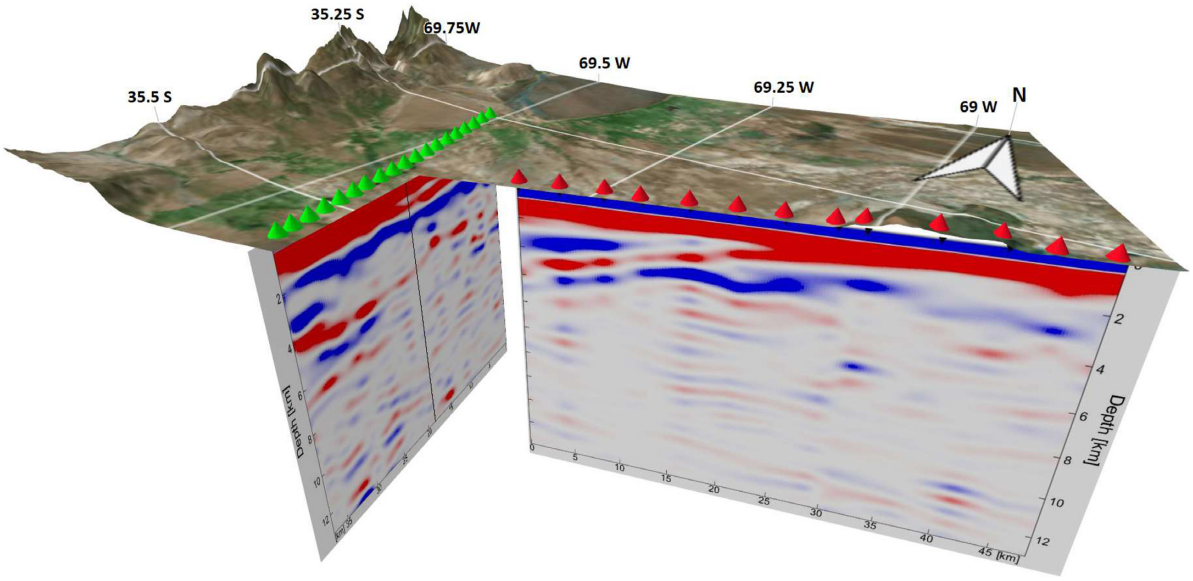

Figure 10. Perspective view of the *PKIKP*-correlation results for the T-array using a 4th-order Butterworth filter between 0.7 and 3 Hz. The color scale ranges from negative amplitudes (blue) to zero (white) to positive amplitudes (red). The cones show the actual location of the stations of the TE- (red) and TN-line (green). The vertical black line on the TN-section represents the projected intersection of the two lines. A non-perspective representation of the results is included in the supporting information (Figs S3 and S4). For the elevation model, SRTM3-data were used (NASA JPL 2013); satellite imagery was retrieved from ESRI (2009).

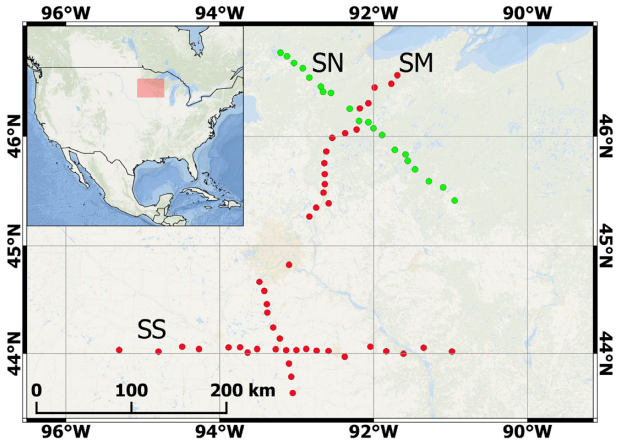

Figure 11. Location of the SPREE array stations inside of the US (red and green). The green dots represent the SN-line, while the red dots display the other US stations of the SPREE-array. The inset shows the relative location of the array. Basemap retrieved from ESRI (2014).

5 DISCUSSION

Based on observations by Verdel *et al.* (2016), who found remarkably high frequencies, up to 8 Hz, originating from a teleseismic (90°) earthquake, this work aimed to quantify these findings and use the high-frequency content to image the shallow crust by means of GloPSI.

Although the results presented in this study have shown that structural information can be retrieved, there is still room for improvement. The observant reader may have noticed that we did not apply any source deconvolution, while eq. 2 states that the signal is convolved with some source–time function. Effectively this means that our final results are somewhat polluted with the source signatures and source-side reverberations of the events. However, by stacking over multiple whitened events, with varying source signatures, the source imprints are largely averaged out, so that mainly the signal associated with the receiver-side structure remains.

As stated before, the time-to-depth-conversions were performed rather crudely and the results could be improved by using more realistic velocity models instead. However, since there are no velocity models available for the investigated structures, such an elaborate assessment is beyond the scope of this paper.

In order to compare the signal of different earthquakes, we introduce f_{max}. This parameter denotes the highest frequency at which the SNR is greater than 5 dB.

While this work has shown the potential of using high-frequency signal, we did not discuss the exact cause of why some earthquakes provide higher frequencies than others, although some general trends at both the receiver—as well as source side were observed. At the receiver side, a connection between the sedimentary basin thickness and f_{max} was observed, with f_{max} decreasing for increasing basin depth. This is likely due to the fact that there is more high-frequency attenuation in the unconsolidated sedimentary unit, compared to the intrusive basement. At the source side, some possible explanations were found during the f_{max} analysis of the US-Array stations. First, it was found that the maximum frequency was decreasing with increasing distance. Second, f_{max} increased with magnitude. Finally, we saw that the maximum frequency increased with increasing hypocenter depth.

To get a better understanding of the increasing f_{max} with magnitude, there are two main contributions that need to be considered. For this we consider the circular fault model by Madariaga (1976) as well as self-similarity between earthquakes (Shearer 2009). Self-similarity implies that the amplitude spectrum can be scaled according to source size (Aki 1967). This means that the spectra of different earthquakes can be scaled in accordance with magnitude, and hence different spectra can safely be compared with each other. With an increase in magnitude, the model predicts an increase of the long-period spectral level, while the corner frequency decreases. At

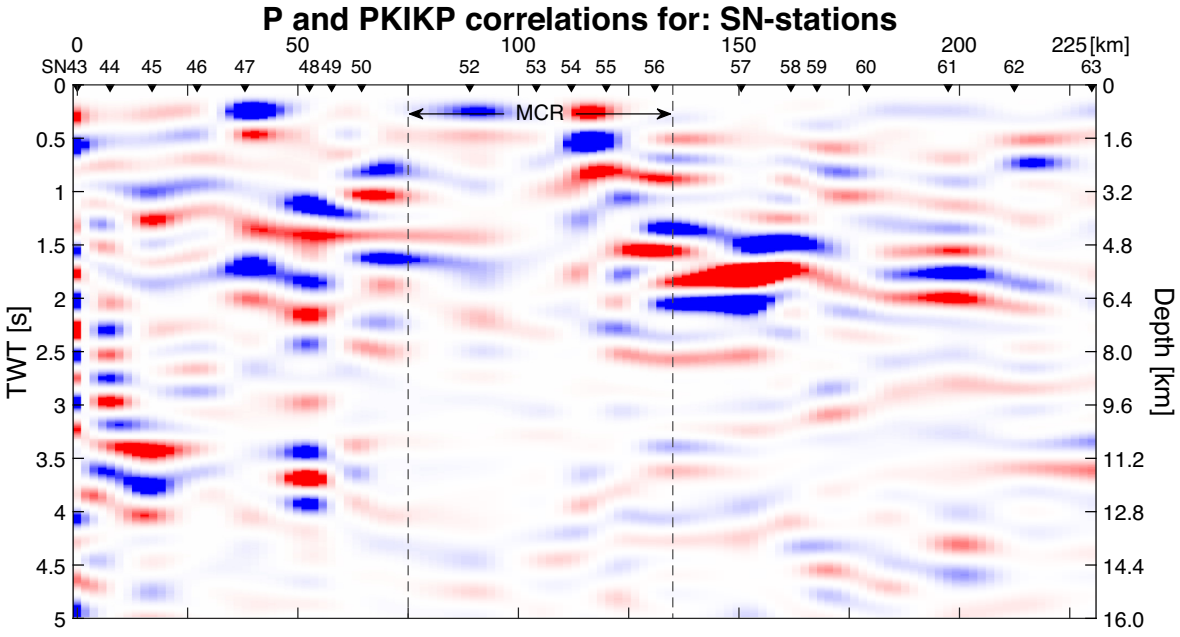

Figure 12. Combined *P*- and *PKIKP*-correlation result for the SN-line, using a 4th-order Butterworth filter between 0.7 and 3 Hz. The left axis shows the TWT depth, the right axis shows the converted depth in km. Negative amplitudes are displayed in blue and positive amplitudes in red. The approximate location of the gravity anomaly of the Midcontinent Rift (MCR) is indicated by the dashed lines.

frequencies above the corner frequency, these effects are competing with each other, because, with increasing magnitudes, the energy in the spectrum for a certain frequency band increases due to a higher long-period spectral level, but decreases due to a lower corner frequency. Fig. 5 shows that the reduction in corner frequency is on average more than compensated by an increase in radiated energy. As a consequence, f_{max} increases with magnitude.

Another question left partly unanswered is which receiver locations would be suitable for the addition of *P*-phases at distances larger than 80°. We found that the SPREE array has a good coverage of events providing these phases, while the Malargüe array was situated in an area with almost no coverage.

Nevertheless, GloPSI yields a clearer image at the Malargüe array than the SPREE array, even though less events were available. This is predominantly due to two reasons. First, the reflecting interfaces below the SPREE array are sometimes far from horizontal, whereas the interfaces below the Malargüe array are only slightly dipping. With our addition of *P*-phases, the illumination was increased from $p \leq 0.04$ s km^{-1} (using only global phases) to $p \leq 0.045$ s km^{-1}. This remains insufficient for imaging steeply dipping interfaces. Secondly, there is a strong contrast in elastic properties expected between the sedimentary overburden and the intrusive basement below the Malargüe array, while the contrasts below the SPREE array are less pronounced, since it mostly consists of volcanic rock at the depths were GloPSI is operating.

Using GloPSI in conjunction with other methods can improve the reliability of shallow crustal imaging results. This was shown for the Malargüe array where GloPSI was used to confirm earlier findings from Nishitsuji *et al.* (2014), and for the SPREE array where it highlighted the presence of the MCR. Another advantage is the cheap and fast computational performance of the method. Finally, the frequency bands (0.7–3 Hz) used in this study are still recorded well with 5 Hz nodal sensors and cabled geophones. This, in combination with only requiring a vertical component, opens the door to applications of GloPSI to large N arrays (dense seismic arrays, e.g. Lin *et al.* 2013).

6 CONCLUSION

This work aimed to quantify high-frequency signal originating from teleseismic, high-magnitude earthquakes and apply GloPSI to image the shallow crust. First, a large amount of waveforms recorded between 2008 and 2018 by 21 USArray stations were analysed. By fitting the SNR and determining the maximum frequency, where the SNR is still above the 5 dB threshold, f_{max} was obtained. It was found that f_{max} increases with magnitude and depth, but decreases with distance. 48.6 per cent of the analysed *P*-, *PKP*- and *PKIKP*-phases showed an f_{max} greater than 3 Hz, 33.2 and 23.7 per cent had a frequency greater than 4 and 5 Hz, respectively. Next, the method was applied to two arrays in order to image the shallow crust. Using data with frequencies between 0.7 and 3 Hz we were able to constrain a sedimentary structure, and identify the imprint of a rifting structure in the upper crust.

The results of this study lead the way for industrial applications of GloPSI, where it can be used in conjunction with other methods to gain a better understanding of the shallow crustal structure, in particular sedimentary basin delineation.

ACKNOWLEDGEMENTS

The authors thank two anonymous reviewers for their valuable comments, which helped to improve both the contents and readability of this manuscript. We also kindly thank Dirk Kraaijpoel (TNO) for valuable discussion on the correlation results.

The facilities of IRIS Data Services and specifically the IRIS Data Management Center were used for access to waveforms, related metadata, and/or derived products used in this study. Data from the TA network were made freely available as part of the

EarthScope USArray facility, operated by the IRIS. IRIS Data Services are funded through the Seismological Facilities for the Advancement of Geoscience and EarthScope (SAGE) Proposal of the National Science Foundation under Cooperative Agreement EAR-1261681.

The authors thank Incorporated Research Institutions for Seismology-Program for Array Seismic Studies of the Continental Lithosphere (IRIS-PASSCAL) for providing the seismic equipment and the Argentine Ministry of Science, Technology, and Production Innovation for the financial support connected to the transport of the equipment. The authors also thank Pierre Auger and the Department of Civil Defense of Malargüe for the help during the data acquisition, as well as Deyan Draganov for making the data publicly available.

Furthermore, the authors thank the contributors to the SPREE-project. SPREE was funded by the National Science Foundation through EarthScope (grant EAR-0952154).

Finally, we thank the contributors to QGIS and the qgis2threejs plugin, for freely distributing their software, which was used to process the geographical information for the figures in the paper.

REFERENCES

Aki, K., 1967. Scaling law of seismic spectrum, *J. geophys. Res.,* **72**(4), 1217–1231.

Becker, G. & Knapmeyer-Endrun, B., 2018. Crustal thickness across the Trans-European Suture Zone from ambient noise autocorrelations, *Geophys. J. Int.,* **212**(2), 1237–1254.

Boatwright, J., 1978. Detailed spectral analysis of two small New York state earthquakes, *Bull. seism. Soc. Am.,* **68**(4), 1117.

Boullenger, B., Verdel, A., Paap, B., Thorbecke, J. & Draganov, D., 2015. Studying CO_2 storage with ambient-noise seismic interferometry: a combined numerical feasibility study and field-data example for Ketzin, Germany, *Geophysics,* **80**(1), Q1–Q13.

Chulick, G.S. & Mooney, W.D., 2002. Seismic structure of the crust and uppermost mantle of North America and adjacent oceanic basins: a synthesis, *Bull. seism. Soc. Am.,* **92**(6), 2478.

Claerbout, J.F., 1968. Synthesis of a layered medium from its acoustic transmission response, *Geophysics,* **33**(2), 264.

Crotwell, H.P., Owens, T.J. & Ritsema, J., 1999. The TauP Toolkit: flexible seismic travel-time and ray-path utilities, *Seism. Res. Lett.,* **70,** 154–160.

Dost, B., Edwards, B. & Bommer, J.J., 2018. The relationship between M and ML: a review and application to induced seismicity in the Groningen Gas Field, The Netherlands, *Seism. Res. Lett.,* **89**(3), 1062–1074.

Draganov, D., Wapenaar, K., Mulder, W., Singer, J. & Verdel, A., 2007. Retrieval of reflections from seismic background-noise measurements, *Geophys. Res. Lett.,* **34**(4).

Draganov, D., Campman, X., Thorbecke, J., Verdel, A. & Wapenaar, K., 2009. Reflection images from ambient seismic noise, *Geophysics,* **74**(5), A63–A67.

Draganov, D., Campman, X., Thorbecke, J., Verdel, A. & Wapenaar, K., 2013. Seismic exploration-scale velocities and structure from ambient seismic noise (>1 Hz), *J. geophys. Res.: Solid Earth,* **118**(8), 4345–4360.

ESRI, 2009. "Imagery" [basemap]. 1:614.291, "World Imagery Map". December 12, 2009. https://server.arcgisonline.com/ArcGIS/rest/services/World_Imagery/MapServer (November 5, 2018).

ESRI, 2014. "Ocean Base" [basemap]. Scale varies, "World Ocean Base". February 24, 2014. https://services.arcgisonline.com/ArcGIS/rest/services/Ocean/World_Ocean_Base/MapServer (November 5, 2018).

Farías, M., Comte, D., Charrier, R., Martinod, J., David, C., Tassara, A., Tapia, F. & Fock, A., 2010. Crustal-scale structural architecture in central Chile based on seismicity and surface geology: implications for Andean mountain building, *Tectonics,* **29**(3).

Gorbatov, A., Saygin, E. & Kennett, B. L.N., 2013. Crustal properties from seismic station autocorrelograms, *Geophys. J. Int.,* **192**(2), 861–870.

Gordon, M.B. & Hempton, M.R., 1986. Collision-induced rifting: the Grenville Orogeny and the Keweenawan rift of North America, *Tectonophysics,* **127**(1-2), 1–25.

Heath, B.A., Hooft, E.E.E. & Toomey, D.R., 2018. Autocorrelation of the Seismic Wavefield at Newberry Volcano: reflections from the magmatic and geothermal systems, *Geophys. Res. Lett.,* **45**(5), 2311–2318.

Hinze, W., Allen, D.J., Braile, L.W. & Mariano, J., 1997. The midcontinent rift system: a major proterozoic continental rift, *Geol. Soc. Am. Special Papers,* **312,** 7–35.

Hutchinson, D.R., White, R.S., Cannon, W.F. & Schulz, K.J., 1990. Keweenaw hot spot: geophysical evidence for a 1.1 ga mantle plume beneath the Midcontinent Rift System, *J. geophys. Res.: Solid Earth,* **95**(B7), 10869–10884.

Keller, G., Russell, D., Hinze, W., Reed, J. & Geraci, P., 1980, Bouguer gravity anomaly map of the east central midcontinent of the United States, US Nuclear Regulatory Commission.

Kennet, B. L.N., 1991. Iaspei 1991 seismological tables, *Terra Nova,* **3**(2), 122–122.

Kennett, B.L.N., Saygin, E. & Salmon, M., 2015. Stacking autocorrelograms to map Moho depth with high spatial resolution in southeastern Australia, *Geophys. Res. Lett.,* **42**(18), 7490–7497.

King, E.R. & Zietz, I., 1971. Aeromagnetic study of the midcontinent gravity high of central United States, *Geol. Soc. Am. Bull.,* **82**(8), 2187–2208.

Kraemer, P., Silvestro, J., Achilli, F. & Brinkworth, W., 2011. Kinematics of a hybrid thick-thin-skinned fold and thrust belt recorded in Neogene syntectonic wedge-top basins, Southern Central Andes between 35 and 36S, Malargüe, Argentina, *AAPG MEMOIR,* **94,** doi:10.1306/13251340M943099.

Lin, F.-C., Li, D., Clayton, R.W. & Hollis, D., 2013. High-resolution 3D shallow crustal structure in Long Beach, California: application of ambient noise tomography on a dense seismic array, *Geophysics,* **78**(4), Q45–Q56.

Madariaga, R., 1976. Dynamics of an expanding circular fault, *Bull. seism. Soc. Am.,* **66**(3), 639–666.

NASA JPL, 2013. NASA Shuttle Radar Topography Mission Global 3 arc second 35 & 36°S, 69 & 70°W, *NASA EOSDIS Land Processes DAAC,* doi:10.5067/MEaSUREs/SRTM/SRTMGL3.003.

Nishitsuji, Y., Ruigrok, E., Gomez, M. & Draganov, D., 2014. Global-phase H/V spectral ratio for delineating the basin in the Malargüe Region, Argentina, *Seism. Res. Lett.,* **85**(5), 1004.

Nishitsuji, Y., Ruigrok, E., Gomez, M., Wapenaar, K. & Draganov, D., 2016. Reflection imaging of aseismic zones of the Nazca slab by global-phase seismic interferometry, *Interpretation,* **4**(3), SJ1–SJ16.

Oren, C. & Nowack, R.L., 2017. Seismic body-wave interferometry using noise auto-correlations for crustal structure, *Geophys. J. Int.,* **208**(1), 321–332.

Phạm, T.-S. & Tkalčić, H., 2018. Antarctic ice properties revealed from teleseismic P wave coda autocorrelation, *J. geophys. Res.: Solid Earth,* doi:10.1029/2018JB016115.

Poli, P., Pedersen, H.A. & Campillo, M., 2012. Emergence of body waves from cross-correlation of short period seismic noise, *Geophys. J. Int.,* **188**(2), 549–558.

Romero, P. & Schimmel, M., 2018. Mapping the basement of the Ebro Basin in Spain with seismic ambient noise autocorrelations, *J. geophys. Res.: Solid Earth,* **123**(6), 5052–5067.

Ruigrok, E. & Wapenaar, K., 2012. Global-phase seismic interferometry unveils P-wave reflectivity below the Himalayas and Tibet, *Geophys. Res. Lett.,* **39**(11).

Ruigrok, E., Campman, X., Draganov, D. & Wapenaar, K., 2010. High-resolution lithospheric imaging with seismic interferometry, *Geophys. J. Int.,* **183**(1), 339–357.

Ruigrok, E., Campman, X. & Wapenaar, K., 2011. Extraction of P-wave reflections from microseisms, *C. R. Geosci.,* **343**(8), 512–525.

Ruigrok, E. *et al.*, 2012. Malargüe seismic array: design and deployment of the temporary array, *Eur. Phys. J. Plus,* **127**(10), 126.

Saygin, E. & Kennett, B.L.N., 2019. Retrieval of interstation local body waves from teleseismic coda correlations, *J. geophys. Res.: Solid Earth,* **124**(3), 2957–2969.

Saygin, E., Cummins, P.R. & Lumley, D., 2017. Retrieval of the P wave reflectivity response from autocorrelation of seismic noise: Jakarta Basin, Indonesia, *Geophys. Res. Lett.,* **44**(2), 792–799.

Shay, J. & Tréhu, A., 1993. Crustal structure of the central graben of the Midcontinent Rift beneath Lake Superior, *Tectonophysics,* **225**(4), 301–335.

Shearer, P.M., 2009. *Introduction to Seismology,* Cambridge University Press.

Stein, S., van der Lee, S., Jurdy, D. *et al.*, 2011. Learning from failure: the SPREE mid-continent rift experiment, *GSA Today,* **21**(9), 5–7.

Storchak, D.A., Schweitzer, J. & Bormann, P., 2003. The iaspei standard seismic phase list, *Seism. Res. Lett.,* **74**(6), 761.

Tibuleac, I.M. & von Seggern, D., 2012. Crust-mantle boundary reflectors in Nevada from ambient seismic noise autocorrelations, *Geophys. J. Int.,* **189**(1), 493–500.

Van der Lee, S., Revenaugh, J., Wiens, D. & Wysession, M., 2013. *Superior Province Rifting Earthscope Experiment (SPREE),* http://www.usarray.org/researchers/obs/flexible/deployments/1116_SPREE/, Accessed: 2018-05-18.

Verdel, A. *et al.*, 2016. Reykjanes ambient noise reflection interferometry, *Proceedings European Geothermal Congress 2016,* Strasbourg, France, 19-24 Sept 2016, ISBN: 978–2–9601946–0–9.

Wapenaar, K., Draganov, D., Snieder, R., Campman, X. & Verdel, A., 2010. Tutorial on seismic interferometry. Part 1 - Basic principles and applications, *Geophysics,* **75**(5), 75A195–75A209.

Weemstra, C., Draganov, D., Ruigrok, E.N., Hunziker, J., Gomez, M. & Wapenaar, K., 2017. Application of seismic interferometry by multidimensional deconvolution to ambient seismic noise recorded in Malargüe, Argentina, *Geophys. J. Int.,* **208,** 693–714.

Wolin, E. *et al.*, 2015. Seasonal and diurnal variations in long-period noise at SPREE stations: the influence of soil characteristics on shallow stations' performance, *Bull. seism. Soc. Am.,* **105**(5), 2433–2452.

Zhan, Z., Ni, S., Helmberger, D.V. & Clayton, R.W., 2010. Retrieval of Moho-reflected shear wave arrivals from ambient seismic noise, *Geophys. J. Int.,* **182**(1), 408–420.

Zhang, H. *et al.*, 2016. Distinct crustal structure of the North American Midcontinent Rift from *P* wave receiver functions, *J. geophys. Res.: Solid Earth,* **121**(11), 8136–8153.

SUPPORTING INFORMATION

Supplementary data are available at *GJI* online.

Figure S1. Flow chart displaying the data acquisition and processing.

Figure S2. Flow chart displaying the selection, processing and autocorrelation of the data.

Figure S3. Non-perspective PKIKP-results of the TE-line, using a 4th-order Butterworth filter between 0.7 and 3 Hz.

Figure S4. Non-perspective PKIKP-correlation results of the TN-line, using a 4th-order Butterworth filter between 0.7 and 3 Hz. The dashed line marks the intersection of the TE-line. The x-axis is reversed to match the perspective view of the TN-line in Figure 8.

Figure S5. Non-perspective PKIKP-results of the TE-line, using a 4th-order Butterworth filter between 0.7 and 3 Hz. The scaled average of all traces has been subtracted from each individual trace.

Figure S6. Non-perspective PKIKP-correlation results of the TN-line, using a 4th-order Butterworth filter between 0.7 and 3 Hz. The scaled average of all traces has been subtracted from each individual trace. The dashed line marks the intersection of the TE-line. The *x*-axis is reversed to match the perspective view of the TN-line in Fig. 8.

Please note: Oxford University Press is not responsible for the content or functionality of any supporting materials supplied by the authors. Any queries (other than missing material) should be directed to the corresponding author for the paper.